Near-field flat-plane images of spherical nanoparticles ☆

W. Bazhan, K. Kolwas

Institute of Physics of Polish Academy of Sciences, Al. Lotników 32/46, 02-668 Warsaw, Poland

Received 4 February 2004; received in revised form 7 September 2004; accepted 12 September 2004

Abstract

The paper is devoted to numerical simulation of homogeneous images of dielectric, semiconductor and metal spherical nanoparticles in a flat plane situated in the near-field region. The influence of the particle radius, the distance to the image plane and the polarization direction of the illuminating light wave on image formation is illustrated on the basis of near-field Mie scattering theory.

© 2004 Published by Elsevier B.V.

1. Introduction

The concept of near-field microscopy is applied in a number of different disciplines, where the benefit of sub-wavelength resolution of near-field optics and simultaneous capability for topography measurement are of interest. Near-field scanning optical microscopy (NSOM) [1–3] and photon scanning tunneling microscopy (PSTM) [4,5] are the most recent scanning probe techniques allowing to image the structure of a sample with nanometer resolution well below the diffraction limit. An optical image can be obtained with the use of a sub-wavelength probe (usually a metal coated tapered optical fiber or appertureless probe) which is scanned close to the sample surface (see [6] for a compact review of methods and references).

However, interpretation of the image still poses some problems in many applications. One of the reasons is, that the electric field at the tip can be highly non-homogeneous. Therefore, the optical characteristics of the probe should be known to understand the image, while it is formed as a convolution of the probe characteristics in the near-field region and the "homogeneous" near-field image of the sample.

An even more fundamental problem is what is the near field "homogeneous" image itself, it is how the near-field distribution characterizing the object looks like. The distribution of the homogeneous light field scattered by a small object in the near-field region differs significantly from the corresponding distribution in the far-field region. Therefore, not only the knowledge of optical characteristics of the probe, but also the homogeneous near field characteristics of the scatterer are necessary for complete interpretation of the image.

The wide field of application of near-field scattering microscopy, gives rise to a renewal of interest in the numerical analysis of fields in the near-field region and in particular in numerical analysis of Mie theory (e.g., [6–10]). The importance of the problem is the motivation for the present, preliminary study. The aim is to illustrate the diversity of the near-field images of small objects illuminated by a homogeneous light field.

As sample objects we use spheres of selected radii and of different optical properties. We show, how the near-field images differ, depending on the distance from the sphere and the polarization of the illuminating light field. The chosen detection geometry (perpendicular to the incoming light field) allows for illustration of the role of the polarization direction of the incoming field with respect to the observation plane. The distribution of electric and magnetic fields of light scattered by a sphere results from Mie theory (e.g., [11–13]). The numerical images of spherical objects with different refraction coefficients are due to the Poynting vector distribution in the plane situated in the near-field region. The obtained near-field images of the object homogeneously created and detected (no subwavelength aperture tip modification) possess considerably different characteristics than the corresponding images in the far field. The diversity of chosen sphere materials allows comparison of the scattering images for a variety of materials starting from dielectric, semiconductor to metallic ones.

2. Scattered near fields

We consider a plane monochromatic light wave illuminating a spherical object of radius a and relative refraction index m which can be a complex number. k is the wave number of the incident light field, and $x = ka$ is the diffraction parameter. Our aim is to reconstruct the image of the particle in the XY plane (see Fig. 1), which is
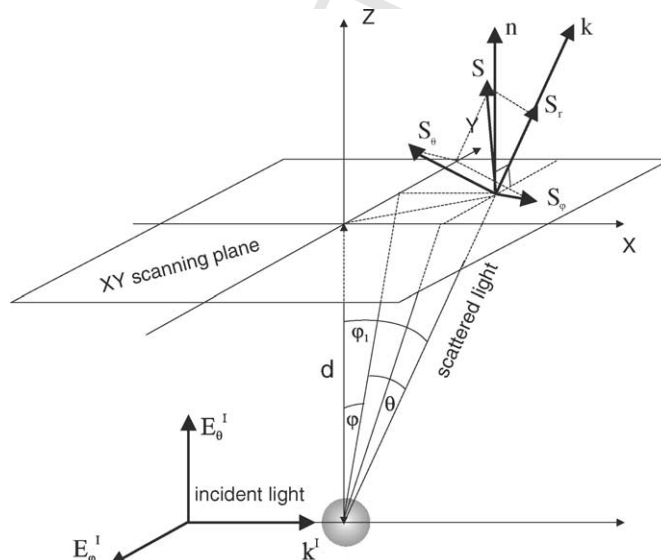
Fig. 1. Definition of the notation used to find the near-field distribution of the normal component $S_n(\theta, \varphi, r)$ of the averaged Poynting vector over the XY scanning plane.

ARTICLE IN PRESS

S0010-4655(04)00461-8/FLA   AID:2773   Vol.•••(•••)   cpc2773   [DTD5] P.3(1-8)
COMPHY:m3 v 1.27 Prn:1/10/2004; 12:26   by:violeta p. 3

W. Bazhan, K. Kolwas / Computer Physics Communications ••• (••••) •••–•••   3

imagined to be scanned along by a detector. r is a distance from the center of the scattering particle to the position (x, y) at the scanning plane.

The components of the electric light field **E** scattered by a sphere in polar coordinates result from Mie theory [12]:

$$E_\theta(\theta, \varphi, r) = \frac{\cos\varphi}{kr} \sum_{n=1}^{\infty} E_n\big(ia_n\xi_n'(kr)\tau_n(\theta) - b_n\xi_n(kr)\pi_n(\theta)\big), \tag{1}$$

$$E_\varphi(\theta, \varphi, r) = \frac{\sin\varphi}{kr} \sum_{n=1}^{\infty} E_n\big(b_n\xi_n(kr)\tau_n(\theta) - ia_n\xi_n'(kr)\pi_n(\theta)\big), \tag{2}$$

$$E_r(\theta, \varphi, r) = \frac{\cos\varphi}{k^2r^2} \sum_{n=1}^{\infty} E_n n(n+1)ia_n\xi_n(kr)\pi_n(\theta)\sin\theta, \tag{3}$$

$$H_\theta(\theta, \varphi, r) = \frac{k}{\omega\mu}\frac{\sin\varphi}{kr} \sum_{n=1}^{\infty} E_n\big(ib_n\xi_n'(kr)\tau_n(\theta) - a_n\xi_n(kr)\pi_n(\theta)\big), \tag{4}$$

$$H_\varphi(\theta, \varphi, r) = \frac{k}{\omega\mu}\frac{\cos\varphi}{kr} \sum_{n=1}^{\infty} E_n\big(ib_n\xi_n'(kr)\pi_n(\theta) - a_n\xi_n(kr)\tau_n(\theta)\big), \tag{5}$$

$$H_r(\theta, \varphi, r) = \frac{k}{\omega\mu}\frac{\sin\varphi}{k^2r^2} \sum_{n=1}^{\infty} E_n n(n+1)b_n\xi_n(kr)\pi_n(\theta)\sin\theta, \tag{6}$$

with

$$E_n = i^n E_0 \frac{(2n+1)}{n(n+1)}, \tag{7}$$

$$a_n = \frac{m\psi_n(mx)\psi_n'(x) - \psi_n(x)\psi_n'(mx)}{m\psi_n(mx)\xi_n'(x) - \xi_n(x)\psi_n'(mx)}, \tag{8}$$

$$b_n = \frac{\psi_n(mx)\psi_n'(x) - m\psi_n(x)\psi_n'(mx)}{\psi_n(mx)\xi_n'(x) - m\xi_n(x)\psi_n'(mx)}, \tag{9}$$

where E_0 is the amplitude of the incident electric field, ω is the frequency of the incident light field, μ is the magnetic permeability of the sphere surroundings ($\mu = 1$ for air), θ and φ are polar zenith and azimuthal angles appropriately.

The angular dependence of the functions $\tau(\theta)$ and $\pi(\theta)$ can be calculated from Legendre polynomials [12]. The functions $\psi_n(x)$ and $\xi_n(x)$ are the Rikkati–Bessel functions. $\psi_l(x) = \sqrt{\frac{\pi x}{2}} J_{l+1/2}(mx)$ and $\xi_l(mx) = \sqrt{\frac{\pi x}{2}} H_{l+1/2}^{(1)}(mx) = \sqrt{\frac{\pi x}{2}}(J_{l+1/2}(mx) - iN_{l+1/2}(mx))$. $J_{l+1/2}(mx)$, $H_{l+1/2}^{(1)}(mx)$ and $N_{l+1/2}(mx)$ are Bessel, Hankel and Neuman cylindrical functions. The prime indicates differentiation with respect to the argument.

3. Intensity of light at the scanning plane

In optics a measure of the light intensity is the magnitude of the Poynting vector, averaged over the time interval which is long compared with the period $2\pi/\omega$ [12]:

$$\mathbf{S} = \tfrac{1}{2}\operatorname{Re}(\mathbf{E} \times \mathbf{H}^*). \tag{10}$$

ARTICLE IN PRESS

S0010-4655(04)00461-8/FLA   AID:2773   Vol.●●●(●●●)   cpc2773   [DTD5] P.4(1-8)
COMPHY:m3 v 1.27 Prn:1/10/2004; 12:26   by:violeta p. 4

4   *W. Bazhan, K. Kolwas / Computer Physics Communications ••• (••••) •••–•••*

The Poynting vector $\mathbf{S}(\theta, \varphi, r)$ for scattered fields Eqs. (1)–(6) reads:

$$\mathbf{S}(\theta, \varphi, r) = \frac{1}{2} \operatorname{Re} \left\{ \left| \begin{matrix} \hat{\mathbf{r}} & \hat{\theta} & \hat{\varphi} \\ E_r & E_\theta & E_\varphi \\ H_r^* & H_\theta^* & H_\varphi^* \end{matrix} \right| \right\} = \hat{\mathbf{r}} S_r(\theta, \varphi, r) + \hat{\theta} S_\theta(\theta, \varphi, r) + \hat{\varphi} S_\varphi(\theta, \varphi, r), \tag{11}$$

where $\hat{\mathbf{r}}$, $\hat{\theta}$ and $\hat{\varphi}$ are the unit vectors of the polar system of coordinates. The magnitude of the Poynting vector $\mathbf{S}$ represents the averaged density of the scattered energy flow, the direction of $\mathbf{S}$ represents the direction of energy propagation.

To obtain the image in the XY plane (see Fig. 1), the distribution of the normal component $S_n(\theta, \varphi, r)$ of the Poynting vector over this plane has to be found:

$$S_n(\theta, \varphi, r) = \hat{\mathbf{n}} \cdot \mathbf{S}(\theta, \varphi, r),$$

where $\hat{\mathbf{n}}$ is the unit vector normal to the XY plane.

If we use the angles θ, φ and φ_1 to parameterize the position (x, y) at the plane XY according to the notation introduced in Fig. 1, the normal component $S_n(\theta, \varphi, r)$ of the averaged Poynting vector can be represented as:

$$S_n(\theta, \varphi, r) = S_r(\theta, \varphi, r) \cos \varphi_1 + S_\theta(\theta, \varphi, r) \sin \theta \cos \varphi - S_\varphi(\theta, \varphi, r) \sin \varphi. \tag{12}$$

The distribution $S_n(\theta, \varphi, r)$ over the XY plane allows numerical simulation of the images formed at that plane with resolution corresponding to the step of the numerical algorithm used (approximately one pixel per one degree).

4. Image simulations and discussion

A series of scattering images for spherical particles of different materials: water ($m = 1.33$), diamond ($m = 2.43$), silicon ($m = 4.42 + i0.02$) and gold ($m = 0.97 + i1.85$) is presented in Figs. 3, 4, 5, and 6 correspondingly. The frequency of light corresponds to the wavelength $\lambda = 488$ nm of the argon-ion laser. The polarization of the incident light field is assumed to be: parallel ($\mathbf{E}_\varphi^I$) or perpendicular ($\mathbf{E}_\theta^I$) to the scanning plane (see Fig. 2 a, b). Images obtained for the polarization perpendicular (parallel) to the scanning plane are presented in the upper (lower) row of a series. Each column of a series corresponds to the same radius a of the scattering sphere and the same distance d to the XY plane. Simulations are made for particles of radii: 100, 200, and 1000 nm. The distance d from the particle center to the detector is chosen to have three values: equal to the particle radius, equal to twice
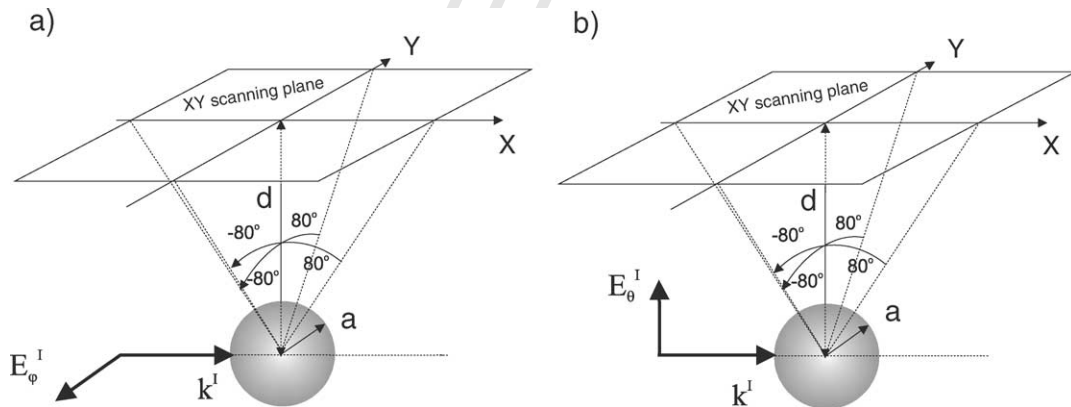

Fig. 2. The studied polarization configurations of the incoming field with respect to the scanning plane (a) E_φ^I scattering geometry (the lower row of images in Figs. 3–6; (b) E_θ^I scattering geometry (the upper row of images in Figs. 3–6).
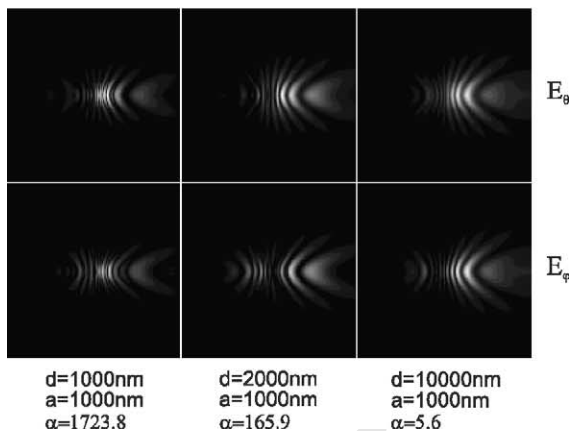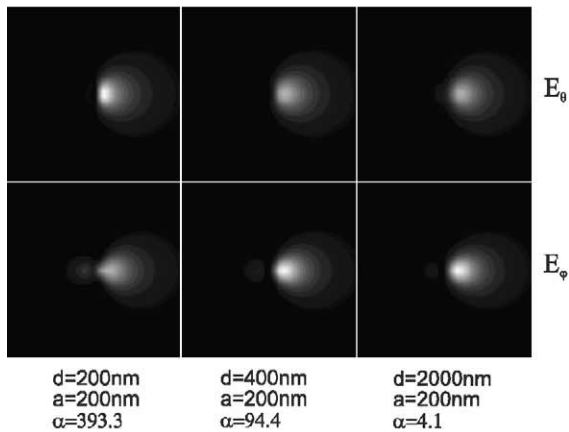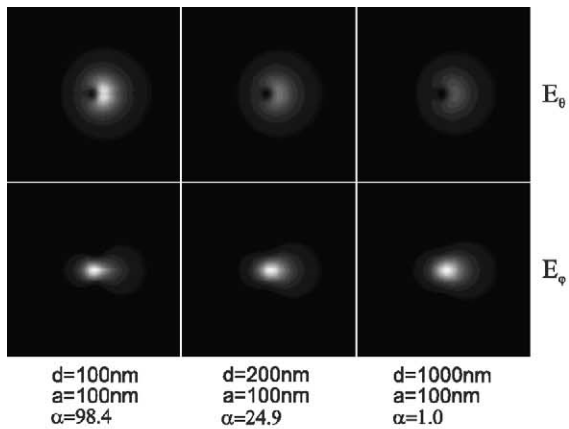
cpc2773

Fig. 3. Images for spherical water particles for chosen radii *a* and chosen distances *d* to the scanning plane. Upper (lower) row: polarization perpendicular (parallel) to the scanning plane. α is the brightness enhancement parameter.
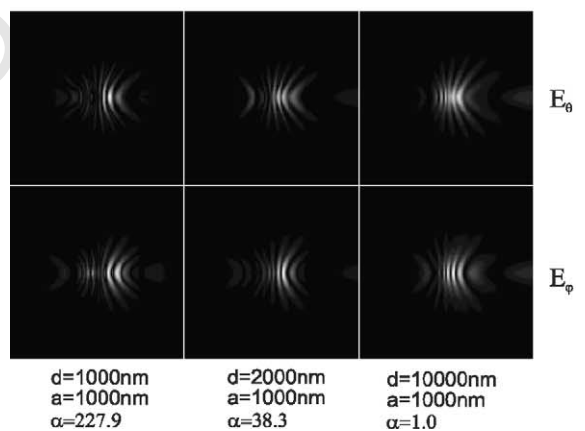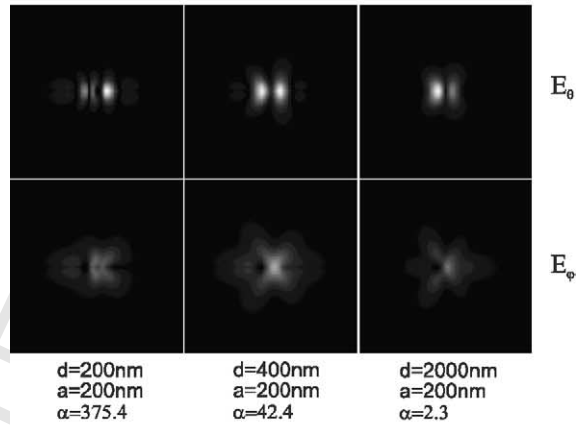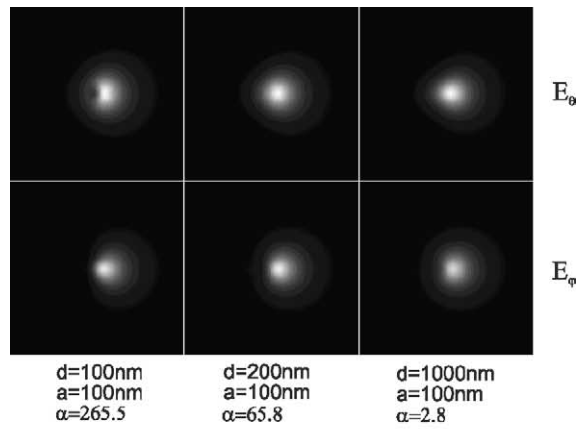

Fig. 4. Images for spherical diamond particles for chosen radii *a* and chosen distances *d* to the scanning plane. Upper (lower) row: polarization perpendicular (parallel) to the scanning plane. α is the brightness enhancement parameter.
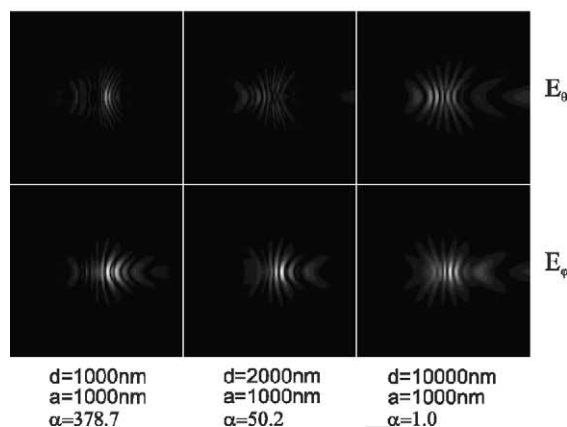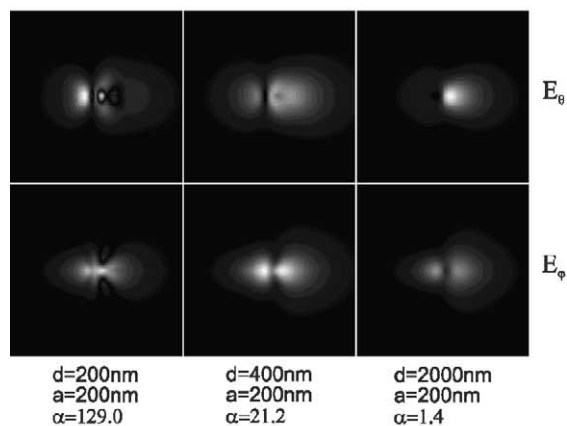
Fig. 5. Images for spherical silicon particles for chosen radii a and chosen distances d to the scanning plane. Upper (lower) row: polarization perpendicular (parallel) to the scanning plane. α is the brightness enhancement parameter.
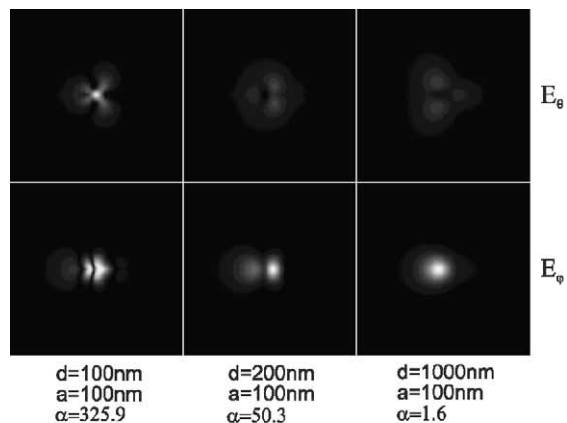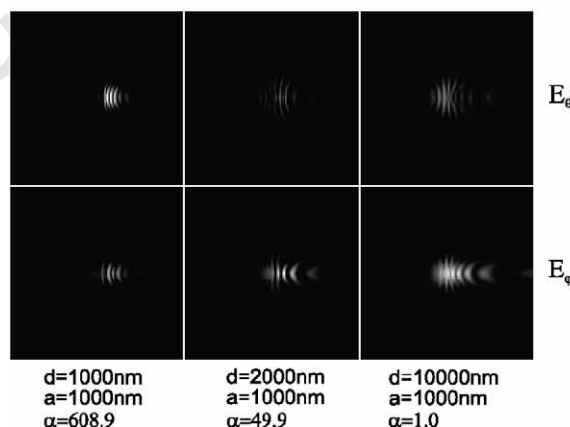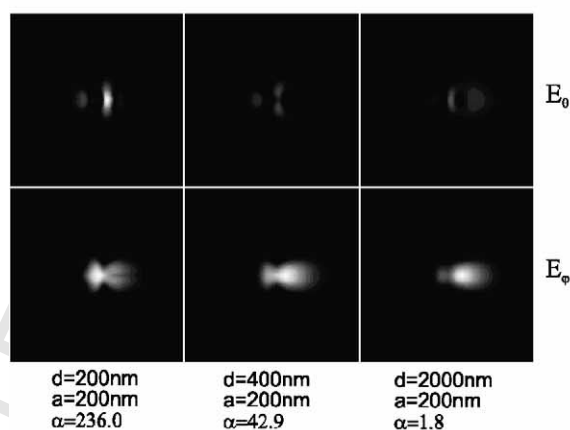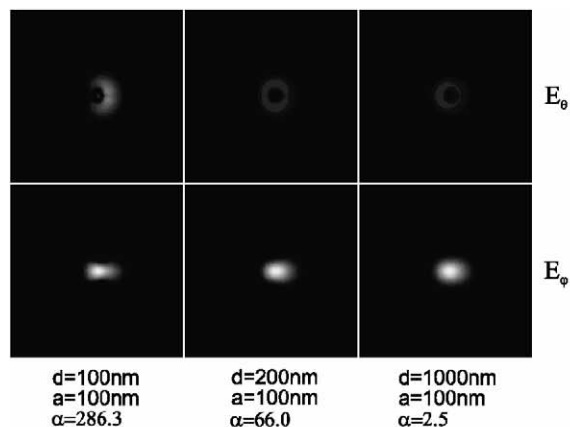

Fig. 6. Images for spherical gold particles for chosen radii a and chosen distances d to the scanning plane. Upper (lower) row: polarization perpendicular (parallel) to the scanning plane. α is the brightness enhancement parameter.

the particle radius and equal to ten times the particle radius (far field approximation). The area of XY scanning plane (the area of the image) is limited by the θ and φ angle ranges ($-80° < \theta < 80°$ and $-80° < \varphi < 80°$ correspondingly (see Fig. 2). Near field image generation algorithm is implemented as a part of ScatLab 1.2 program. Last version of ScatLab 1.2 application is available on http://www.scatlab.com.

Near field images differ significantly from those of the far field region. The difference is due to the fact, that the radial components of the electric and the magnetic fields E_r and H_r in near-field region are comparable in magnitude to the transverse components E_θ, H_θ, E_φ and H_φ. At larger distances E_r and H_r values decay drastically (E_r, H_r in proportion to $1/r^2$ while E_θ, E_φ, H_θ, H_φ only in proportion to $1/r$) and the scattered wave gains transverse character. Therefore, the near-field Poynting vector is significantly distorted in comparison to the far-field Poynting vector. In the far field zone, the vector $\mathbf{S}$ for scattered fields is directed in the radial direction: there exists only one real non-zero radial component of $\mathbf{S} = S_r(\theta, \varphi, r)\hat{\mathbf{r}}$. However, in the near field region, all three non-zero components of $\mathbf{S}$ can contribute to the image, while $(\mathbf{E} \times \mathbf{H}^*)_\theta$, $(\mathbf{E} \times \mathbf{H}^*)_\varphi$ and $(\mathbf{E} \times \mathbf{H}^*)_r$ can contain real terms in general (no approximation is made concerning the smallness of particle radius a in comparison with the distance r [7]).

The brightness of images at distances d nearest to the particle is appreciably enhanced in comparison with images at larger distances. The measure for the enhancement is the parameter α introduced for each image series. $\alpha = 1$ is attributed to the weakest image brightness in far-field region of each series. To keep all the numerical images of one series visible in graphical form, the brightness of each image presented in Figs. 3–6 is rescaled one-to-one by a corresponding factor $1/\alpha$.

5. Conclusions

Conventional optics deals with electromagnetic waves in the far field region at large distances from the object. In the far field approximation, the scattered electromagnetic waves are transverse, so only the transverse field components contribute to the image. In conventional Mie scattering the far-field plane wave Mie solutions are used. However, the complete Mie solutions contain the nonzero radial field components, which contribute to the image causing distortion of the averaged Poynting vector with respect to the radial direction.

The present study is aimed to illustrate the images of spherical particles of different material properties in a plane situated in the usual scanning plane of the PSTM techniques. On the basis of exact Mie theory, we develop an image generating algorithm which is implemented in computer code appropriate for spherical particles of radii up to $\sim$10000 nm. The diversity of near-field images of small spherical particles illuminated by a homogeneous light field is presented for dielectric, semiconductor and metal spherical particles. Simulations are made for several particle radii and particle distances from the scanning plane. The obtained near-field images of the object homogeneously created and detected (no subwavelength aperture tip modification) possess considerably different characteristics than the corresponding images in the far field.

The near-field images of a stand alone particle could be of interest in the field of photon scanning tunneling microscopy (PSTM) as a help in a preliminary interpretation of properties of a scattering particle. However, the PSTM images are much more complex since the presence of a detector perturbs the homogeneous near-field characteristics of the scattering object. If it is the surface of the lens situated in the image plane, one have to include multiple scattering of the electromagnetic field between the surface and the object. The analysis of that complex problem will be the subject of the future paper.

We note, that our procedure is not adequate for imaging a particle located on a plane substrate and illuminated by an evanescent wave. Homogeneous and evanescent waves are scattered in different manner (e.g., [14]). Therefore, if a particle scatters an evanescent wave, the image could differ significantly from the image based on near-field Mie scattering theory because of the spatially asymmetric distribution of an evanescent wave and multiple interaction between a particle and a substrate boundary [15]. In this case more complex models have to be used [16–18].

cpc2773

References

[1] F. Zenhausern, M.P. O'Boyle, H.K. Wickramasinghe, Appl. Phys. Lett. 65 (1994) 1623.

[2] N.H.P. Moers, R.G. Tack, N.F. van Hulst, B. Bölger, J. Appl. Phys. 75 (1994) 1254.

[3] Y. Inouye, S. Kawata, Opt. Lett. 19 (1994) 159.

[4] R.C. Reddick, R.J. Warmack, D.W. Chilcott, S.L. Sharp, T.L. Ferrell, Rev. Sci. Instrum. 61 (1990) 3669.

[5] R.C. Reddick, R.J. Warmack, T.L. Ferrell, Phys. Rev. B 39 (1989) 767.

[6] J.T. Krug II, E.J. Sánchez, X.S. Xie, J. Chem. Phys. 116 (2002) 10895.

[7] J. Noh, J. Ji, W. Jhe, J. Korean Phys. Soc. 36 (2000) 67.

[8] D. Ganic, X. Gan, M. Gu, Opt. Comm. 216 (2003) 1.

[9] M. Quinten, A. Pack, R. Wannemacher, Appl. Phys. B 68 (1998) 87.

[10] C. Liu, T. Kaiser, S. Lange, G. Schweiger, Opt. Comm. 117 (1995) 521.

[11] M. Born, E. Wolf, Principles of Optics, Pergamon, Oxford, 1970.

[12] G.F. Bohren, D.R. Huffman, Absorption and Scattering of Light by Small Particles, Wiley, 1983.

[13] U. Kreibig, M. Vollmer, Optical Properties of Metal Clusters, Springer, 1995.

[14] V.A. Sterligov, P. Cheyssac, S.I. Lysenko, R. Kofman, Opt. Comm. 186 (2000) 27.

[15] M. Gu, P. Ke, J. Appl. Phys. 88 (2000) 5415.

[16] A. Doicu, Y. Eremin, T. Wriedt, Opt. Comm. 182 (2000) 281.

[17] A. Doicu, Y. Eremin, Comput. Phys. Comm. 134 (2001) 1.

[18] T. Wriedt, A. Doicu, Opt. Comm. 152 (1998) 376.